Palaeogeography, Palaeoclimatology, Palaeoecology 471 (2017) 181–195

Contents lists available at ScienceDirect

Palaeogeography, Palaeoclimatology, Palaeoecology

journal homepage: www.elsevier.com/locate/palaeo

Paleosol-based paleoclimate reconstruction of the Paleocene-Eocene Thermal Maximum, northern Argentina

Elizabeth Andrews [a], Timothy White [b,*], Cecilia del Papa [c]

[a] Department of Geosciences, The Pennsylvania State University, University Park, PA 16802, United States
[b] Earth and Environmental Systems Institute, The Pennsylvania State University, University Park, PA 16802, United States
[c] CICTERRA -F. C. E. F y N., CONICET-Universidad Nacional de Córdoba, Av. Vélez Sarsfield 1611, X5016GCA, Córdoba, Argentina

ARTICLE INFO

Article history:
Received 28 July 2016
Received in revised form 26 January 2017
Accepted 31 January 2017
Available online 02 February 2017

Keywords:
PETM
Paleosols
Paleoclimate reconstruction
CIE
Argentina

ABSTRACT

The Paleocene-Eocene Thermal Maximum (PETM) is a well-documented, relatively short-lived, warm episode in Earth history. Previous studies completed on marine and continental strata spanning the PETM have focused on understanding the magnitude of warming and other atmospheric changes. These studies, completed largely in the Northern Hemisphere, report warming that ranged from 4 to 8 °C above mean annual paleotemperatures prior to warming.

In this study, paleosols in the Salta Basin, northern Argentina, are used to reconstruct paleoprecipitation rates and mean annual paleotemperatures of the Southern Hemisphere from before, during and after the PETM. Carbon isotope data are used to: 1) identify the horizon in which the PETM and other Eocene hyperthermals are recorded; and, 2) to interpret perturbations of the global carbon cycle during the PETM. At the height of the PETM, paleoprecipitation proxies indicate ~1500 mm of annual rainfall and a temperature increase of ~5 °C from pre-PETM values. Carbon isotope data records three negative carbon isotope excursions during the PETM in this region, suggesting the possibility of three distinct, rapid releases of isotopically depleted carbon into the ocean-atmosphere system. The results presented here are one of only a few paleoclimate reconstructions from continental sediments spanning the PETM in the Southern Hemisphere.

1. Introduction

The Paleocene-Eocene Thermal Maximum (PETM) represents an abrupt but relatively short-lived period of warming in Earth history. The PETM occurred ~55.9 million years ago (Charles et al., 2011) and spanned ~170,000 years (Röhl et al., 2007). Many studies have been completed to determine the magnitude of associated climate change and its timespan. Most studies have shown a temperature change of 4–8 °C above mean annual paleotemperatures (e.g., Kennett and Stott, 1991; Wing et al., 2005; Zachos et al., 2003), and indicate that Earth was mostly free of continental glaciers at this time (Miller et al., 1987). Along with elevated temperatures, an enhanced and accelerated hydrological cycle has been proposed during this time (Domingo et al., 2009; Schmitz and Pujalte, 2007).

The late Paleocene-early Eocene Earth was similar to present in some respects: early Eocene paleogeography was similar to modern geography with the exception of the absence of several prominent mountain ranges and the presence of shallow seas. For example, uplift of the Andes Mountains was just beginning (Gregory-Wodzicki, 2000), and other mountain ranges such as the Himalaya had not yet arisen (Aitchison et al., 2007). The lack of continental scale glaciation caused higher eustatic sea level, thus shallow seas existed in Europe and northern Africa (Blakey, 2014). Further similarities can be found in modern and Paleogene flora and fauna. Since the Cretaceous, angiosperms have been the dominant plant type, similar to modern flora, and the Paleogene marks the beginning of mammals as a dominant fauna (Woodburne et al., 2009). Overall, Paleogene geography, flora and fauna were more similar to global conditions today than during many past episodes of global warmth.

The PETM is considered by many paleoclimatologists to be a good analog for ongoing climate change because the calculated rate and amount of carbon released to the PETM atmosphere may be similar to ongoing anthropogenic releases. No other episode of post-Cretaceous global warmth appears to have occurred at such an accelerated rate of change (Zeebe et al., 2016).

Some of the most prominent studies of the PETM have been from deep-sea cores, showing that sea surface temperature increased by 5 °C in the tropics and as much as 9 °C at high latitudes, while the deep ocean temperature increased by 4–5 °C (Zachos et al., 2005). Many studies of PETM terrestrial strata have also been completed, notably in the Bighorn Basin, Wyoming, but also in other locations in the United States and Europe. In the Bighorn Basin and nearby localities, many different approaches have been applied to understand the PETM climate. Leaf margin analysis was used to estimate a PETM temperature

* Corresponding author.
E-mail address: tswhite@essc.psu.edu (T. White).

http://dx.doi.org/10.1016/j.palaeo.2017.01.042
0031-0182/

of 19.8 °C, a nearly 5 °C change from before the PETM (Wing et al., 2005). Carbon and oxygen isotope data was analyzed by Koch et al. (1995, 2003), demonstrating that terrestrial carbon reservoirs were linked to marine reservoirs, observable as coeval shifts in the isotopic records in both realms. Oxygen isotope values from mammal teeth enamel and aragonite bivalve shells indicate that extensive rainout occurred in the Paleogene Bighorn Basin, suggestive of an intensified hydrologic cycle during peak warmth (Koch et al., 1995).

Studies of paleosols spanning the PETM in the Bighorn Basin (e.g., Kraus and Riggins, 2007; Adams et al., 2011; Kraus et al., 2013) have contributed greatly to understanding PETM climate conditions, and provide evidence for a very dry environment leading up to and during the PETM followed by wetter conditions during recovery from PETM warmth (Kraus et al., 2013). In North Dakota, Clechenko et al. (2007) studied clay mineralogy, major oxides, and bulk organic carbon isotopic analyses of PETM paleosols and found evidence for intensified continental weathering and that the paleohydrology in that region varied greatly (Clechenko et al., 2007). Other studies completed in France and Spain interpret higher seasonal precipitation rates leading to the deposition of very thick coarse-grained deposits that are considered to have been "megafans" or very large alluvial fans (Domingo et al., 2009; Schmitz and Pujalte, 2007).

A paleosol-based study in Texas showed that before the PETM smectite dominated the clay content of soils, but during the PETM a shift to dominantly kaolinite occurred (White and Schiebout, 2008). The kaolinite shift has been observed in other localities and indicates increased weathering due to increased humidity that led to increased hydrolysis in the soils (Clechenko et al., 2007; Robert and Kennett, 1994). Elevated atmospheric CO_2 probably increased carbonic acid delivery to soils, resulting in increased weathering (White and Schiebout, 2008).

Atmospheric changes during the PETM are recorded alongside a worldwide negative carbon isotope excursion (CIE) (Kennett and Stott, 1991). The CIE shows a −2.5 to −4‰ shift during the PETM in both continental and marine records (e.g., Garel et al., 2013; Kennett and Stott, 1991; Smith et al., 2007). The CIE is well enough established that when combined with other stratigraphic constraints, it can be used as a tool to refine chronostratigraphy and the correlation of stratigraphic sections, an approach used in this paper.

The negative CIE is attributed to a large release of isotopically depleted carbon into the ocean-atmosphere system. Many mechanisms have been proposed for this release including the dissociation of methane hydrates from the seafloor (e.g. Dickens et al., 1995), explosive volcanism (e.g. Bralower et al., 1997), comet impact (e.g. Kent et al., 2003), and worldwide wildfires (e.g. Moore and Kurtz, 2008). Considering these hypothesized causes, modelers have estimated the amount and timing of carbon released to the atmosphere. Some studies indicate that carbon release occurred slowly over a long period (Cui et al., 2011), while others support rapid releases (Bowen et al., 2015). The amount varies slightly with different models but many converge on a value between 2000 and 4400 Pg of isotopically depleted carbon from methane to produce the PETM CIE (Bowen et al., 2004; Cui et al., 2011; Zachos et al., 2005; Zeebe et al., 2016). Most researchers conclude that methane oxidation caused PETM greenhouse warming.

This paper presents a reconstruction of paleotemperatures and paleoprecipitation rates from a terrestrial site in northern Argentina spanning the PETM. Carbon isotope data and the implications of multiple isotope excursions are discussed as well. The focus is to understand the climatic and hydrologic changes experienced before, during and after the PETM in the Southern Hemisphere and the relationship to observations made in the Northern Hemisphere.

2. Background

Two stratigraphic sections were measured, described and sampled for this study: a site called Tin Tin in El Parque Nacional de los Cardones, and El Obelisco, on the outskirts of Cafayate (Fig. 1). The study sites are located in the western part of the Salta Basin, northwestern Argentina.

Mesozoic extensional basins were stranded as failed rifts in South America during the breakup of Gondwana, and sediment sourced from the proto Andes Mountains filled the basins (del Papa, 1999). The Salta Basin is one of these, filled with over 5000 meters (m) of Cretaceous through Paleogene sedimentary rock called the Salta Group. There are three main stratigraphic subdivisions of Salta Group strata including the Pirgua, the Balbuena and the Santa Barbara Subgroups. The Pirgua Subgroup is comprised of strata deposited during rifting while the Balbuena and Santa Barbara Subgroups record early and late post-rift sedimentation, respectively (Marquillas et al., 2005). The late post-rift Santa Barbara Subgroup includes strata spanning the PETM. The Santa Barbara Subgroup contains three lithological units: the Mealla, Maíz Gordo and Lumbrera Formations (Fms; Fig. 2). The three units are characterized by a predominance of relatively coarse-grained fluvially deposited strata (Marquillas et al., 2005). Overview images of the study sections are displayed in Fig. 3.

The Mealla Formation (Fm) consists of erosive-based, fine to medium grained fining-upward sandstones with trough and tabular cross-stratification and current ripple marks, interbedded with thick red siltstone beds that contain carbonate nodules and occasional rhizoliths. The Mealla Fm is interpreted to have been deposited by a wandering river system as described by Wooldridge and Hickin (2005) with large floodplains on which paleosols formed; thin sandstones within siltstones are consistent with crevasse splay deposition. Our field descriptions of paleosols in the formation indicate that they are dominantly red, clayey sandstone to clayey pebble conglomerate with calcic nodules and vertic structures that we classify as calcic vertisols to vertic calcisols using the paleosol classification schema of Mack et al., 1993 (further presented in Mack and James, 1992).

The Maíz Gordo Fm conformably overlies the Mealla Fm and is dominated by erosive-based coarse-grained trough cross-bedded sandstone and conglomerate beds. The meter-scale sandstones are interpreted to represent bar-fill channels of a braided river (del Papa, 1999). The Maíz Gordo Fm has generally fewer and thinner fine-grained beds than the under and overlying formations. In some locations in the basin, the Maíz Gordo Fm consists of lacustrine siltstones, limestones and shales (del Papa, 1999). Paleosols in the Maíz Gordo Fm described by us are dominantly white to light gray, fine to coarse clayey sandstone, with fewer vertic structures and fewer calcic horizons. A prominent greenish gray clayey (kaolinitic) sandstone with abundant red to blue to purple and yellow reticulate hematite/siderite nodules exists at the top of the formation. We have classified these paleosols as gleyed oxisols, using the paleosol classification schema of Mack et al., 1993 (further presented in Mack and James, 1992), based on the presence of kaolinite and hematite, the absence of clay illuviation; we modify oxisol as gleyed based on the presence of drab colored to yellow and red mottles, and siderite.

The Lumbrera Fm unconformably overlies the Maíz Gordo Fm, and consists of three distinct sub-units. The lowest is primarily trough cross-bedded sandstone with interbedded decimeter to meter thick red siltstones and fine-grained sandstones, and some massive red siltstones with calcareous nodules. The midsection contains several-meter-thick trough cross-bedded coarse-grained sandstone to conglomerate beds. The upper portion is composed of trough and tabular cross-stratified sandstone beds, interlayered with massive red siltstones and mudstones with thin fine-grained, parallel-laminated sandstones. Marquillas et al. (2005) interpreted the Lumbrera Fm as having been deposited by a sandy meandering fluvial system with extensive alluvial plains. Our field descriptions of paleosols within the formation indicate a dominance of red claystones with abundant calcic nodules and vertic structures, and occasional gray mottles, interpreted to have formed in a relatively dry paleoenvironment, and classified as calcic vertisols using the paleosol classification schema of Mack et al., 1993 (further presented in Mack and James, 1992).

Until very recently, the primary age constraints on Salta Basin strata were derived solely from biostratigraphic and palynostratigraphic

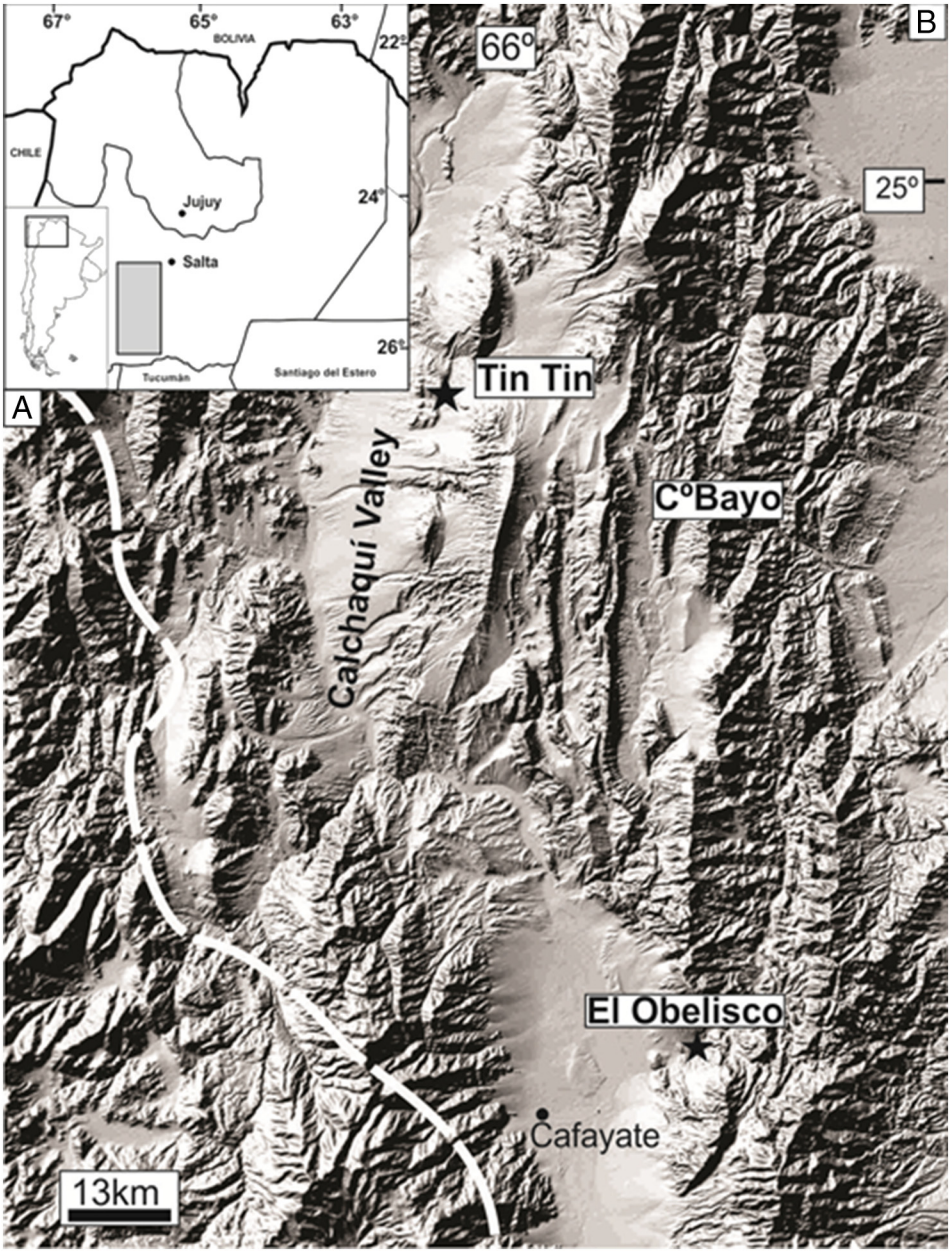

Fig. 1. A) Location map showing the area in B, note bold line: Argentina border with Bolivia and Chile; thinner lines: provincial borders. B) Digital topography (SRTM data) of the southern part of the Central Andes, showing the sampled locations (stars). Dashed white line indicates the southwestern border of the Cretaceous-Eocene Salta Basin.

studies. Palynostratigraphy of the Santa Barbara Subgroup indicates that the Mealla and Maíz Gordo Fms date to the Selandian and Thanetian respectively; the final two ages of the Paleocene Epoch. The Lumbrera Fm has been dated using palynostratigraphy and mammal fossils to the Eocene Epoch (Quattrochio et al., 2005). More recently, a study completed in nearby coeval sections applied paleomagnetic results to determining the age of Santa Barbara Subgroup strata (Hyland et al., 2015). The study found that the age of the Mealla Fm spans from 59.4–58.9 Ma in the mid Paleocene (Hyland et al., 2015), in agreement with palynostratigraphic age determinations. The site studied by Hyland et al. (2015) lies between the two sites presented here (Co Bayo in Fig. 1), so the paleomagnetic ages provide some age constraints for our study sections.

3. Methods

Paleosols were described including measurements of depth to a calcic horizon, thickness of a calcic horizon, and the diameter and stage of development of calcareous nodules. Samples of the paleosol matrix and nodules were collected and brought back to The Pennsylvania State University for geochemical and isotopic analyses. In the lab, carbonate nodules were drilled with a Dremel tool to collect samples for carbon and oxygen isotopic analysis. The powders were analyzed on an Elemental Analyzer-Isotope Ratio Mass Spectrometer (EA-IRMS) in the Department of Geosciences. The (1σ) error associated with these measurements is $\pm 0.098‰$ based on replicate analyses of an in-house carbonate standard.

Paleosol matrix was ground by mortar and pestle and passed through a 100-mesh sieve for bulk organic carbon isotope and major oxide analysis. Carbon isotope measurements of bulk organic matter were made on matrix samples after carbonate was dissolved with hydrochloric acid. Samples were rinsed with deionized water and dried before analysis. The error associated with measuring organic matter carbon isotopes was determined to be $\pm 0.11‰$ by replicate analyses of an in-house standard. Major oxide analysis required fusion of the ground

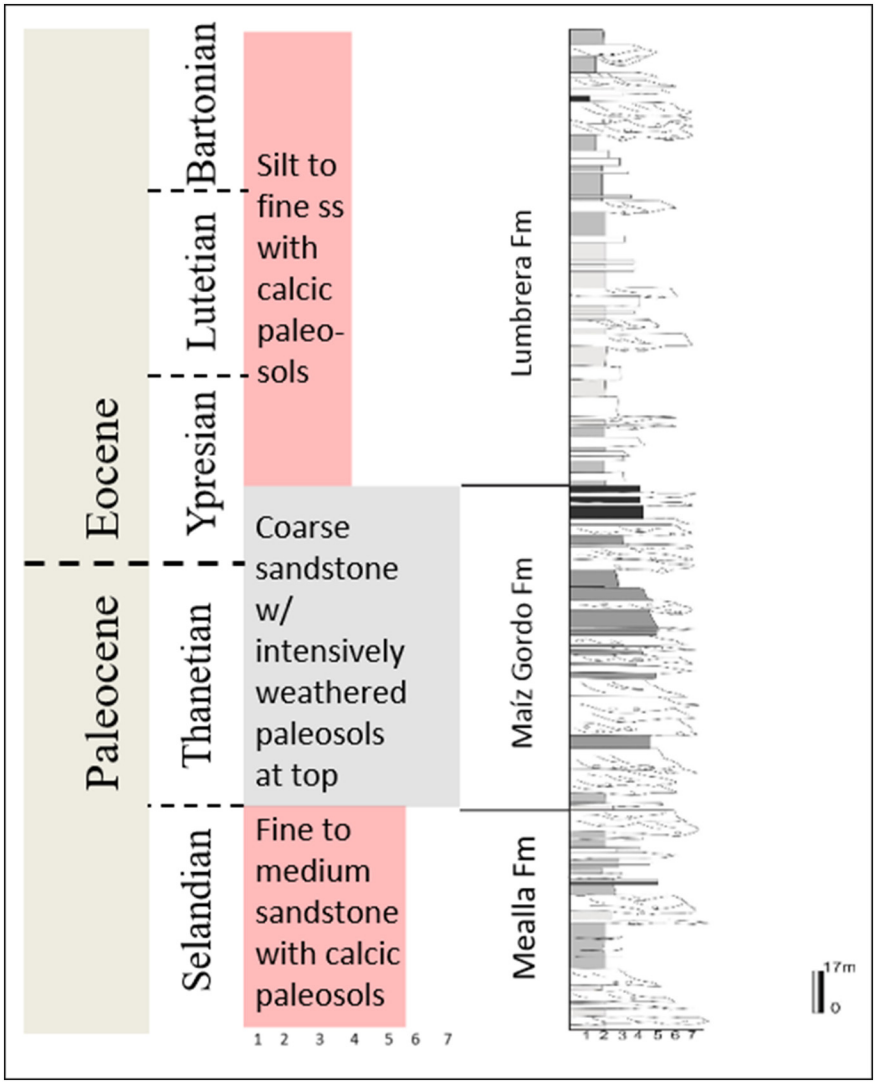

Fig. 2. Composite stratigraphic section for the study interval with simplified colored blocks on the left to represent average grain size and color of each formation of the Santa Barbara Subgroup. Grain size is marked on the right by a number series: 1 = mudstone, 2 = siltstone, 3 = fine sandstone, 4 = medium sandstone, 5 = coarse sandstone, 6 = fine conglomerate, and 7 = coarse conglomerate. Ages and Epochs are marked with dashed lines indicating uncertainty in the exact placement of the boundaries and are provided from Marquillas et al. (2005) and Quattrochio et al. (2005).

sample with lithium metaborate followed by dissolution in 5% nitric acid. Samples were analyzed for major oxides using Inductively Coupled Plasma Atomic Emission Spectroscopy. Error associated with the measurement of weight percent of major oxides is ±2.2%. Data from major oxide analyses were converted from weight percent to molar percent to calculate the various paleoclimatic parameters discussed below.

Previously established weathering proxies and mean annual precipitation proxies were used to calculate paleoprecipitation rate. Sheldon et al. (2002) reported a correlation between the chemical index of alteration (CIA) minus potash (CIA-K) and the mean annual precipitation (MAP) of North American soils. The reported relationship is $P = 221.12e^{0.0197(CIA-K)}$ where CIA-K is $Al_2O_3/(Al_2O_3 + CaO + Na_2O) * 100$ as defined by Maynard (1992). The error associated with this paleoprecipitation calculation is ±182 mm (Sheldon et al., 2002). The first paleoprecipitation calculation reported in this paper was completed using the relationship from Sheldon et al. (2002). A second paleoprecipitation calculation was completed using the relationship between CALMAG and precipitation presented by Nordt and Dreise (2010). CALMAG is an additional weathering index that looks at four major base-forming oxides and better fits the weathering of clay rich soils than the Sheldon et al. (2002) equation. The equation for CALMAG is $Al_2O_3/(Al_2O_3 + CaO + MgO) * 100$, and the relationship between CALMAG and MAP is $P = 22.69 * (CALMAG) - 435.8$. The error associated with CALMAG-based MAP calculation is ±108 mm (Nordt and Dreise, 2010). A field-based paleoprecipitation proxy, depth-to-calcic horizon, defined by Retallack (2005), was also used to calculate a paleoprecipitation rate. The relationship is defined as $P = 137.24 + 6.45D + 0.013D^2$ where P is mean annual precipitation in millimeters and D is the depth to the calcic horizon in centimeters. The error associated with this is ±147 mm.

Paleotemperature was also calculated using geochemical proxies. Sheldon et al. (2002) reported the following equation: $T = -18.516(S) + 17.298$, where $S = (Na_2O + K_2O)/Al_2O_3$. This is a general relationship between the ratio of oxides and the temperatures of soils, and can be applied to most soil (and paleosol) orders, with the exception of deeply weathered kaolinitic soils of tropical regions (Sheldon et al., 2002). The error associated with the relationship between mean annual paleotemperature and this ratio is ±4.4 °C (Sheldon et al., 2002). Gallagher and Sheldon (2013) published a paleothermometer for forest paleosols specifically; by focusing on a distinct set of paleosols rather than all 12 orders, paleotemperature may be better constrained. The relationship published in their paper is: $T = -2.74 * \ln(PWI) + 21.39$; PWI (Paleosol Weathering Index) $= 100 * (4.20 * Na + 1.66 * Mg + 5.54 * K + 2.05 * Ca)$. The Paleosol

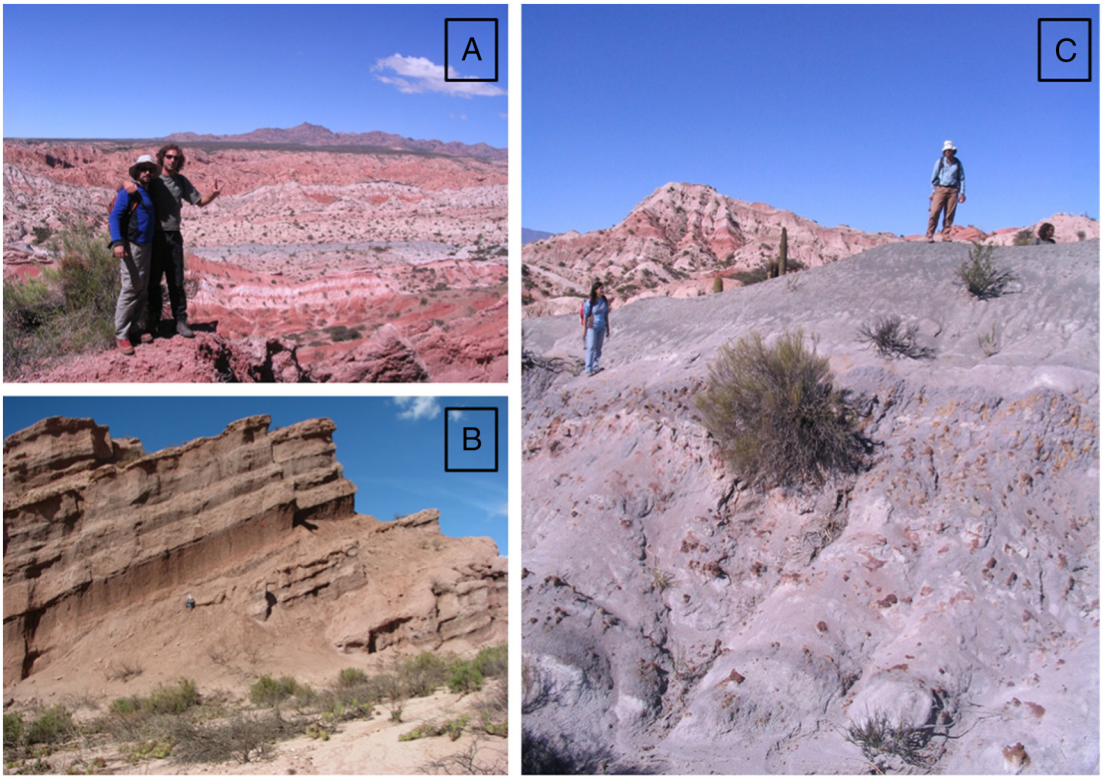

Fig. 3. Landscape photographs from the Salta Basin field areas showing: A) overlook view to the southwest of the Tin Tin badland exposures of the mid-Paleocene Mealla (foreground, red and white strata), late Paleocene-early Eocene Maíz Gordo (middle ground, white to bluish gray), early to middle Eocene Lumbrera (top marked by Argentinian geologist's outstretched hand, white to reddish), and the overlying Quebrada de los Colorados Formations (background, red; not considered in this study); B) outcrop section of the lower Lumbrera Formation at the El Obelisco locale. Note brownish red silty claystone paleosols intercalated with tan channel-form sandstones, and person for scale (middle left); C) white to bluish gray clayey sandstone paleosol with purple and red reticulate hematite/siderite nodules from the Tin Tin badlands. Geologist at top of section marks the top of the organic matter PETM CIE reported here. (For interpretation of the references to color in this figure legend, the reader is referred to the web version of this article.)

Weathering Index (PWI) is an additional weathering proxy developed by Gallagher and Sheldon (2013) that calculates relative loss of major base cations. The error in mean annual paleotemperature associated with the Gallagher and Sheldon (2013) equation is ±2.1 °C. The Sheldon et al. (2002) equation was used to calculate paleotemperature for the samples before and after the PETM, while the Gallagher and Sheldon (2013) equation was used to calculate paleotemperature for the paleosols in the Maíz Gordo Fm. This approach is based on the classification of Mealla and Lumbrera Formation paleosols as calcic vertisols to vertic calcisols, Maiz Gordo Formation paleosols as gleyed oxisols, and the relevant limitations of the PWI and Sheldon et al. (2002) equations described above.

4. Results

A composite section of the two field sites was created by aligning marker beds and combining the stratigraphic description from each site into one stratigraphic column (see Figs. 2 and 9). Carbon isotope data from the composite section is presented in Figs. 4 and 9.

In the lowest 75 m of the section, the carbonate-carbon isotope values are relatively constant with variation within ~2‰ except for an ~3‰ excursion at ~25 m. The average carbonate isotopic value in these lower 75 m is ~−7.9‰. Between ~75 m and ~240 m of the section, the strata do not contain carbonate nodules. Above 240 m, carbonate-carbon isotope values generally display a 2‰ variation. At ~340 m, another large shift of ~−6‰ is observable. The average isotopic composition of the carbonate samples from the uppermost portion of the section is −8.5‰.

The organic matter carbon isotopic profile is characterized by a paucity of data in the lowest 100 m of the section but in the little data that exists, and similarly to the carbonate data, the variation in $\delta^{13}C$ values is ~2‰, with an average value ~−21.4‰. Between 100 and 210 m in the section the strata do not contain appreciable organic matter. At 210–240 m, the organic matter carbon isotope values vary much more significantly, on the order of 6‰. Over these 30 m of the section the organic matter carbon isotope values range from −22‰ to ~−28‰. Three large shifts can be observed here and each large shift gradually becomes isotopically depleted before a rapid recovery to an initial relatively enriched value. The first shift is ~−3‰ in magnitude while the second and third shifts are ~−5 to 6‰.

Above 240 m, the organic carbon isotope data is slightly more variable than the carbonate data set displaying ~3‰ variation. At 340 m, similarly to the carbonate data, the most enriched value attained in this portion of the section is followed upsection by a negative shift of ~5‰. The average $\delta^{13}C$ value from organic matter carbon in the 240–370-meter interval is −20.8‰. At the top of the section, ~370 m, an ~−6‰ shift exists in the organic carbon isotope data. Over the entire section, the most negative value attained is −27.7‰ and the average background organic carbon isotope value is about −21‰ (determined by averaging values from below and above the excursions).

The Chemical Index of Alteration (CIA) is a proxy for weathering that recognizes that hydrolytic weathering of labile minerals causes progressive transformation into clay minerals. Kaolinite, with a CIA value of 100, represents the highest degree of weathering (for comparison, the CIA value of illite falls in the range 75–90, muscovite = 75, feldspar = 50, fresh granite = 45–55, and fresh basalt = 30–45; Nesbitt and Young, 1982; Fedo et al., 1995). Values generally increase from 40 to 60 in the first 100 m of the section, averaging ~56 (Fig. 4). No samples were collected between 100 and 210 m in the section, due to lack of paleosols. At 210 to 240 m in the section, the CIA values increase significantly and some approach 100. Above 240 m in the section, the CIA values become

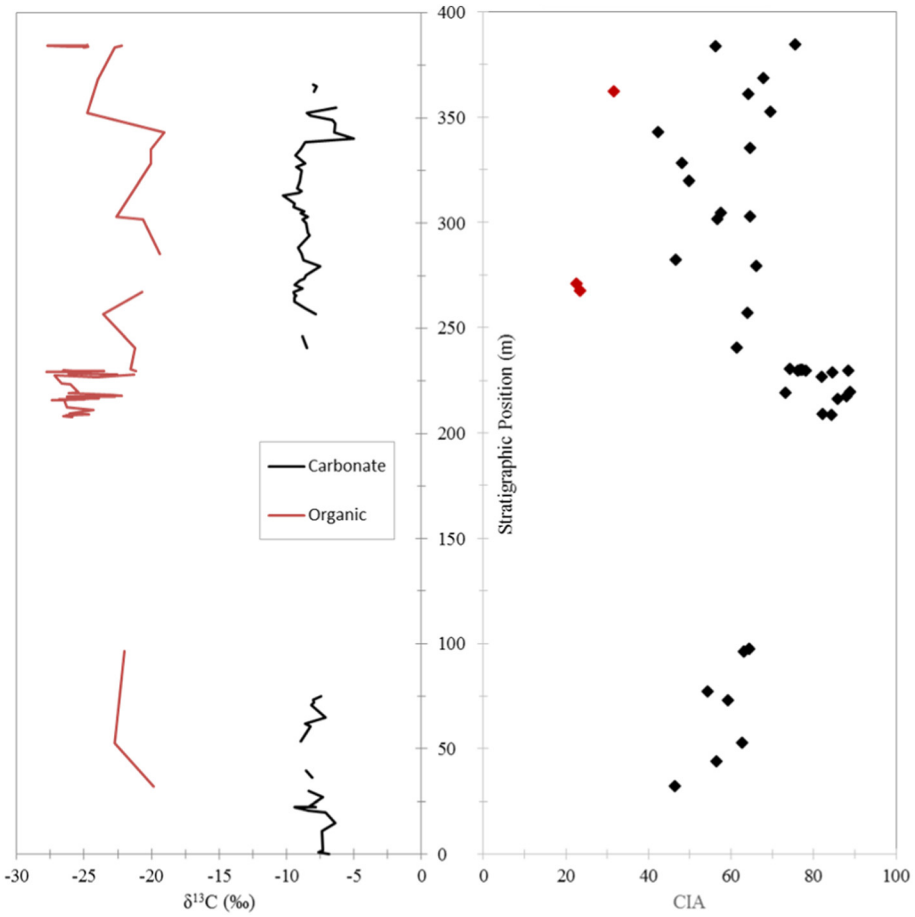

Fig. 4. Carbon isotope data and CIA values plotted against stratigraphic position. Black lines connect carbon stable isotope data collected from carbonate. Red lines connect carbon stable isotope data collected from organic material. Black diamonds represent calculated CIA values from oxide molar percent values presented in Appendix 1. The three red diamonds indicate samples that contained high CaO values after acidification. (For interpretation of the references to color in this figure legend, the reader is referred to the web version of this article.)

more scattered but are generally lower than the values observed in the 210–240-meter interval. The values increase slightly in the uppermost portion of the section.

Major oxide data are presented in Appendix 1A. CIA-K and CALMAG values were calculated for each sample using the major oxide data (Fig. 5). CIA-K and CALMAG are two different weathering proxies but the

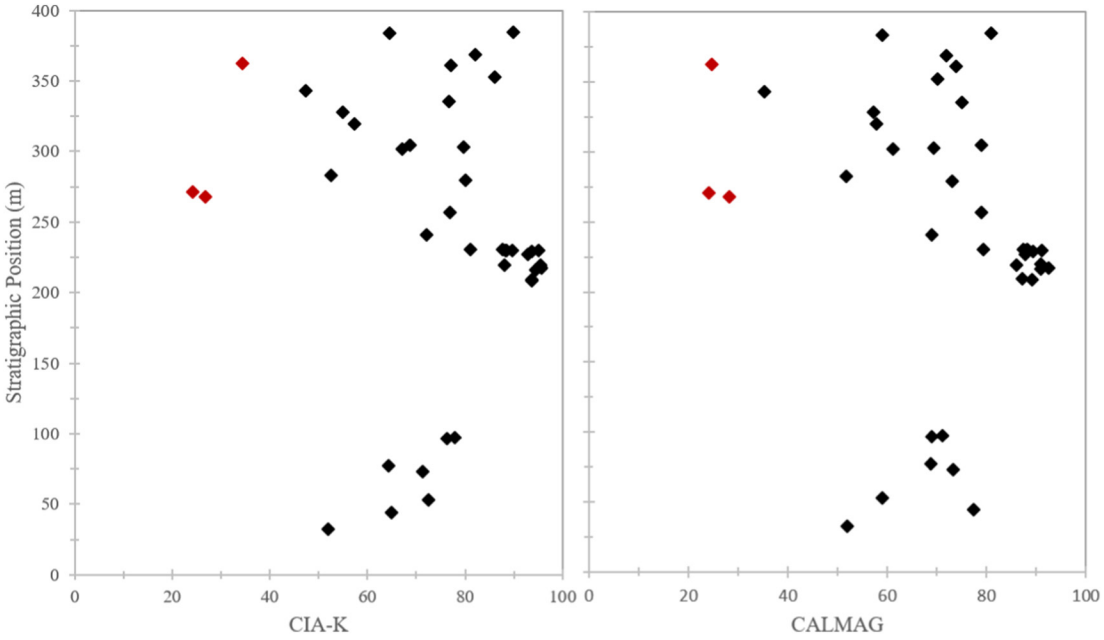

Fig. 5. Plot of CIA-K values and CALMAG values against depth in the section. Red diamonds indicate samples that contained a significant amount of CaO after acidification. (For interpretation of the references to color in this figure legend, the reader is referred to the web version of this article.)

plots in Fig. 5 show similar trends. In the lowest 100 m of the section, the weathering proxies begin at ~50 and steadily increase to 80 at ~80 to 100 m. The CALMAG values have one unusually high data point at ~45 m. In the 210–240 m interval, both the CIA-K values and the CALMAG values approach 100. Above 240 m, the data display substantial scatter but are generally lower than values seen at 240 m. The CIA-K values show a gradual increase towards the top of the section. There are several unusually low values at ~260, 345 and 360 m in both the CIA-K and CALMAG data sets. The average CIA-K value above 250 m is ~80 while the average CALMAG value in the same portion of the section is ~70.

The depth-to-calcic horizon is a field measurement made from paleosols. Fig. 6 shows that the depth to calcic horizon for the study paleosols is highly variable. In the first 75 m, there is a slightly increasing trend in the depth-to-calcic horizon. From about 75–240 m, no paleosols with calcic horizons were found. In the upper portion of the section, there are two peaks at about 275 and 310 m. These peaks represent a depth of 170 and 180 cm to the calcic horizon. Above 325 m, the average depth-to-calcic horizon decreases to about 25–50 cm.

A general paleothermometry ratio from Sheldon et al. (2002) is used for paleotemperature calculations of the study paleosols. This ratio is $(Na_2O + K_2O)/Al_2O_3$ and can be used between 2 and 20 °C; above 20 °C essentially all of the K and Na have leached from the soil. In Fig. 7, the ratio is ~0.4 for the first 100 m of the section with only slight variation. At 210–240 m, the values vary much more significantly with a cluster around 0.1 and a slightly smaller cluster of data around 0.2. Above 240 m, the values increase to ~0.4 and then steadily decrease towards the top of the section. At the top of the section the paleotemperature ratio is ~0.2.

In the lower 100 m of the section, the PWI value is approximately ~44. Between 200 and 235 m in the section, the PWI values average ~20. 20. From ~235 m through the top of the section, the PWI value varies between 40 and 55 but average ~46. PWI values above 60 indicate that the weathered material is indistinguishable from parent material. In this section, there are several outliers with PWI values above 60. These anomalously high values are caused by high CaO and MgO content in the samples. (See Fig. 8.)

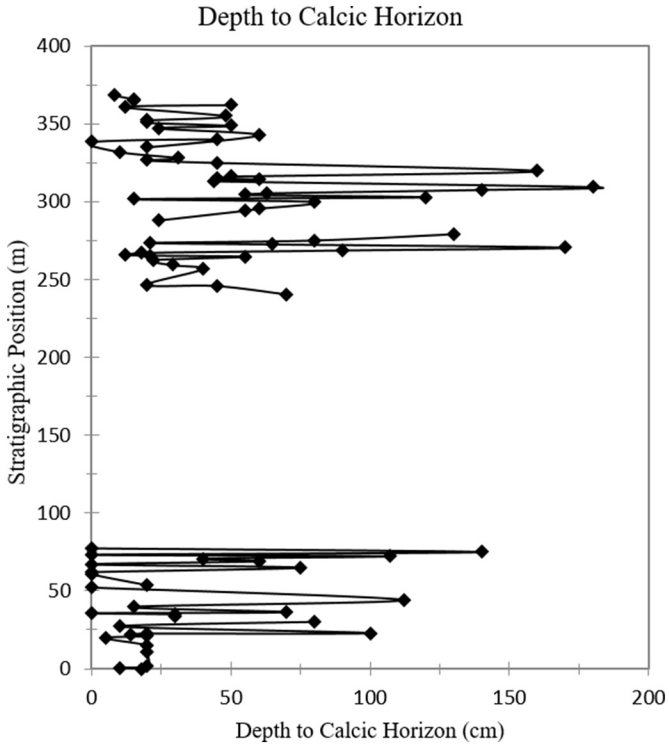

Fig. 6. Plot of depth to calcic horizon against the stratigraphic position of each sample.

5. Discussion

5.1. Chronostratigraphy

Based on the results of earlier research summarized in Fig. 2, the Mealla and Maíz Gordo Fms represent the final two ages of the Paleocene Epoch, and the beginning of the Eocene Epoch; therefore the Maíz Gordo Fm is expected to contain the PETM. The presence of an ~ −6‰ CIE at the top of the Maíz Gordo Fm, presented in Fig. 9, is highly suggestive of the presence of the PETM in the formation. However, the lack of appropriate lithologies for isotopic analyses in the lower portion of the Maíz Gordo Fm made it difficult to determine if the entire CIE has been captured in these strata. The best age constraints we have for the data presented here is: 58.9 Ma for the base of the Maíz Gordo Fm, based on the paleomagnetic data of Hyland et al. (2015); and whatever can be determined through comparison of our CIE with other published well-constrained late Paleocene to early Eocene CIEs.

The organic matter CIE from the top of the Maíz Gordo Fm contains three shifts, the oldest of which is a −3‰ shift, while the overlying second and third shifts are each about −5–6‰; each shift is followed by an enrichment in isotopic composition, probably indicative of a rapid recovery from the carbon cycle perturbing event. A close inspection of field lithological descriptions of the sampled intervals indicates that these shifts cannot be tied to facies changes.

Bowen et al. (2015) observed two distinct excursions in paleosol carbonate-carbon isotope data associated with the PETM CIE. They interpreted these distinct excursions to represent two rapid releases of isotopically depleted carbon into the ocean-atmosphere system. Their first excursion, or pre-onset excursion (POE), is an ~−3‰ excursion that precedes the PETM CIE. Their second excursion is the main event: the −6‰ PETM CIE (Bowen et al., 2015).

The top of the Maíz Gordo Fm presents three excursions similar to those reported by Bowen et al. (2015). These excursions may be considered in two ways. First, there may have been additional excursions that occurred prior to deposition of strata that record the −6‰ CIE at this field site if the record presented here is incomplete due to the lack of analyzable material in much of the Maíz Gordo Fm below the CIE. In this situation, an upper bound of 55.75 Ma (from Charles et al., 2011) may be placed on the recovery of the CIE observed at the top of the Maíz Gordo Fm. However, this interpretation is confounded by the second, preferred interpretation of the carbon isotope record described here. The second, preferred interpretation is that the initial −3‰ shift in the Maíz Gordo Fm correlates to the −3‰ POE shift identified by Bowen et al. (2015), and that the overlying −6‰ excursion in the Maíz Gordo Fm matches the primary −6‰ CIE observed at ~1505 m in the Bowen et al. (2015) outcrop section (see their Fig. 1). Notably different from the Bowen et al. (2015) carbon isotope data is the presence of a third excursion in the Salta Basin record, of equal magnitude to the second excursion. In this second interpretation, only the lowest portion of the PETM CIE has been recorded in the Argentina section, which can be reliably dated to ~55.9 Ma using the age constraints from Charles et al. (2011). The overlying Lumbrera Fm unconformably overlies the Maíz Gordo Fm in the study section, and the rapid recovery observed at the top of the Maíz Gordo Fm may mark a hiatus in the upper portion of the global PETM CIE.

If the correlation between the −3‰ excursion in Argentina and the Bowen et al. (2015) POE is correct, and if the unconformity has truncated the top of the Maíz Gordo Fm excursion, then additional younger excursions may have marked the development of the PETM but are not recorded in this section. Independent of the two different interpretations, the results presented here indicate that an additional excursion to those identified by Bowen et al. (2015) may characterize the PETM CIE. Each excursion followed by a rapid recovery to near background

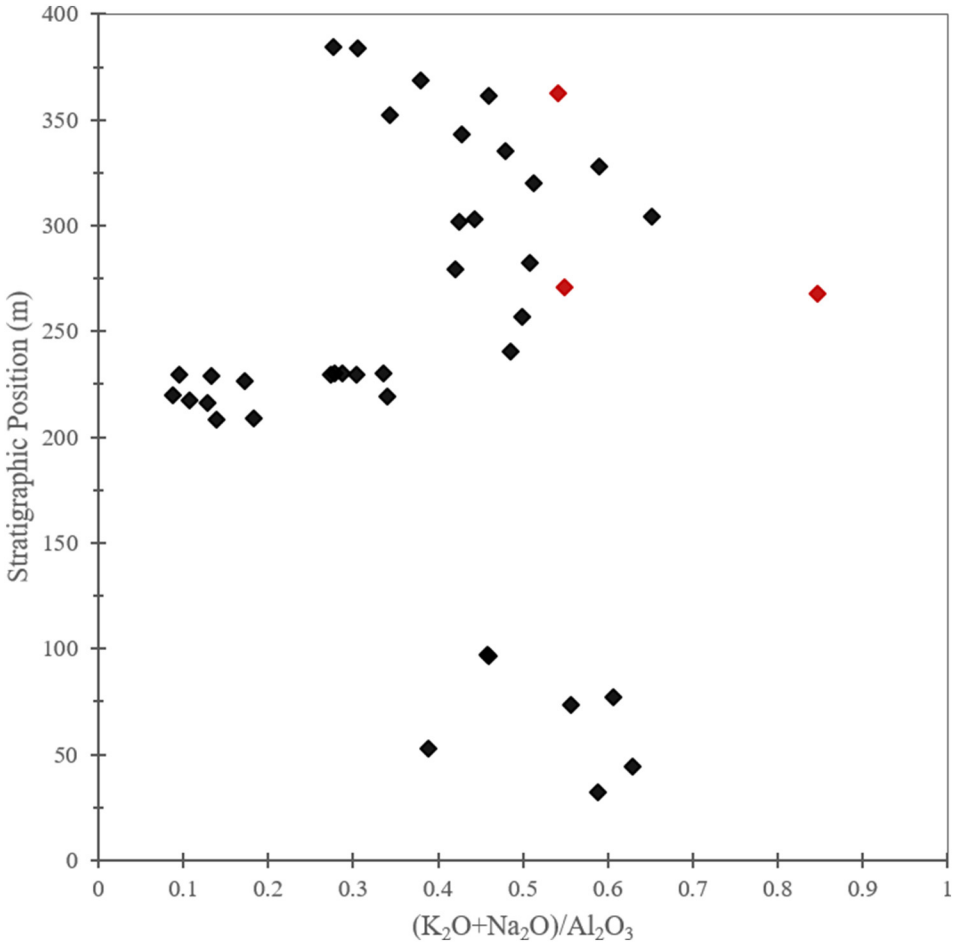

Fig. 7. Plot of the paleothermometry ratio from Sheldon et al. (2002) against depth in the section. Red diamonds indicate samples that contained a significant amount of CaO after acidification. (For interpretation of the references to color in this figure legend, the reader is referred to the web version of this article.)

levels may represent multiple discrete and very rapid releases of isotopically depleted carbon into the ocean-atmosphere system (Bowen et al., 2015) that collectively comprise the PETM CIE.

The early Cenozoic is marked by small but notable negative CIEs that have been interpreted to represent a series of short-lived episodes of warming, or hyperthermals; of these, the PETM is the most conspicuous and well-studied (Zachos et al., 2010). The additional notable CIEs observed in the Mealla and Lumbrera Fms (−3‰ shift at ~25 m in the Mealla Fm; in the Lumbrera Fm, ~−3‰ shifts at ~260 and 305 m, and ~−6‰ shifts at ~350 and ~370 m; see Fig. 9) likely mark hyperthermal events.

Hyland et al. (2015) identified two hyperthermals in the Mealla Fm, one being the Mid Paleocene Biotic Event (MPBE) that exists immediately prior to the Selandian/Thanetian boundary. The single Mealla Fm excursion described in this study (the −3‰ shift at ~25 m) is of the same magnitude as the Hyland et al. (2015) MPBE, suggesting a possible correlation between the two. These observations are consistent with studies of Eocene marine records discussed next.

The additional excursions in the Lumbrera Fm above the PETM CIE are as difficult to constrain chronostratigraphically as excursions in the Mealla Fm. The age of the top of the Lumbrera Fm is considered to be 54.5 Ma based on paleomagnetic studies completed by Sempere et al. (1997), while del Papa et al. (2010) placed the lower boundary of the Lumbrera Fm at approximately 46 Ma based on mammal fossils. The latter research indicates the presence of an ~10 million year hiatus above the unconformable Maíz Gordo/Lumbrera Fm boundary. Due to an overall lack of deep incision at the formation boundary and the presence of transitional facies across the boundary, we prefer the Sempere et al. (1997) age of 54.5 Ma as a more probable age constraint for the Lumbrera Fm.

From marine carbon isotope records, Cramer et al. (2003) and Nicolo et al. (2007) each described four Early Eocene hyperthermal events, while Zachos et al. (2010) focused on two of the Eocene hyperthermals: the Eocene Thermal Maximum 2 (ETM2) and Eocene Thermal Maximum 3 (ETM3). Each of the four Eocene excursions described in those studies is ~−1‰ in magnitude, notably smaller than the Lumbrera Fm CIEs. The difference in magnitude of the excursions challenges correlation between Lumbrera Fm CIEs and known Eocene hyperthermal events, noting though that terrestrial CIEs are typically larger than their coeval marine counterparts. Nonetheless, the match in total number of CIEs in the Lumbrera Fm and early Eocene marine strata is notable, and along with the lack of excursions in middle Eocene strata provides good support for the early Eocene age assignment of Sempere et al. (1997) for the upper part of the Lumbrera Fm.

Alternatively, if the del Papa et al. (2010) age assignment of ~46 Ma for the base of the Lumbrera Fm is correct, then the four Lumbrera Fm CIEs must record carbon cycle perturbations during the Middle to Late Eocene. However, CIEs during this time are less frequent, show less depletion, and are not as well characterized, so correlation between sections of these ages and the Salta Basin sections are unlikely to be valid. We consider the record of CIEs presented here to perhaps provide a better reckoning of chronostratigraphy than any presented in the existing literature, and conclude that the Sempere et al. (1997) age assignment is closest to an accurate pick.

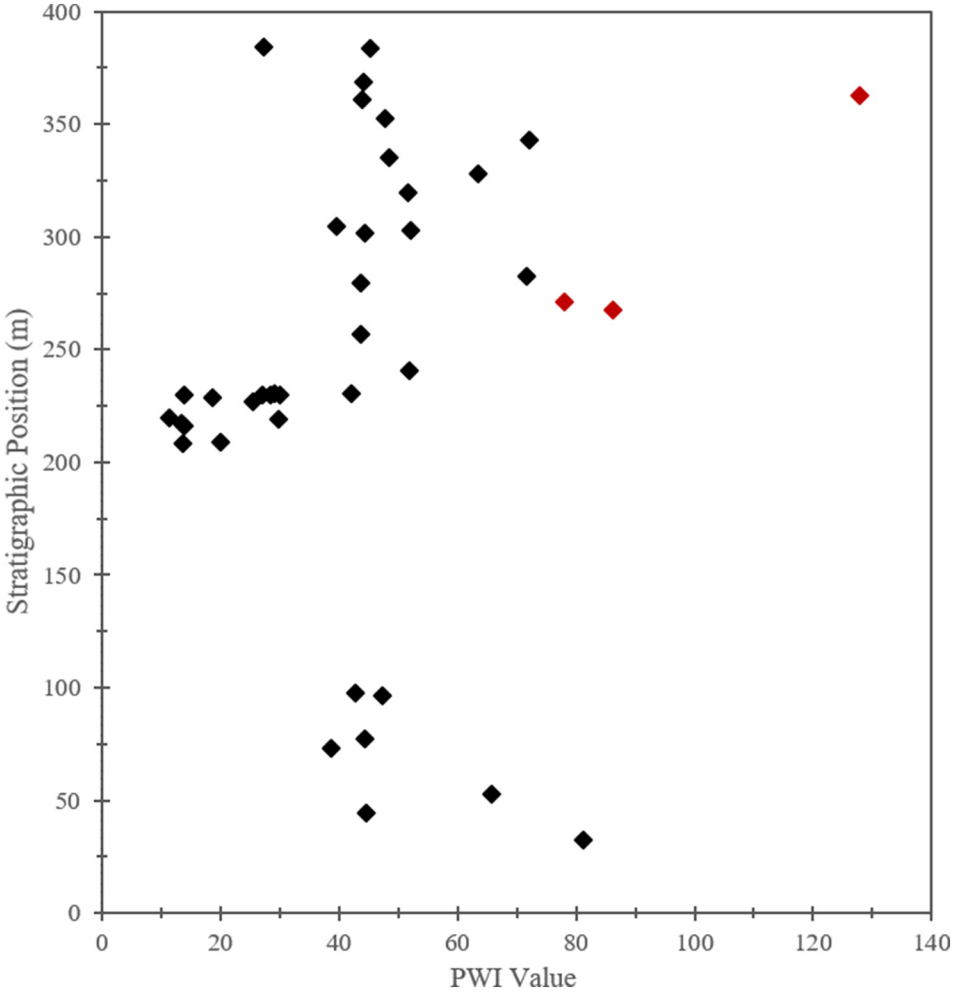

Fig. 8. Plot of Paleosol Weathering Index against depth in the section. Red diamonds indicate samples that contained significant CaO after acidification. (For interpretation of the references to color in this figure legend, the reader is referred to the web version of this article.)

5.2. Paleoprecipitation

The CIA, CIA-K, and CALMAG values are weathering proxies in which higher values indicate increased weathering. The CIA-K and CALMAG proxies have been correlated with mean annual precipitation rates using modern soils (Sheldon et al., 2002; Nordt and Dreise, 2010). Calculated paleoprecipitation rates for the Paleogene strata, Salta Basin, are presented in Fig. 10. During the PETM, spanning 210–240 m in the section, ~1500 ± 182 mm/yr of precipitation fell according to the CIA-K proxy, while the CALMAG proxy predicts slightly more precipitation at ~1600 ± 108 mm/yr. We consider the CIA-K proxy to be more appropriate for use with the paleosols that span the PETM, as the CALMAG proxy is specifically for Vertisols (Nordt and Dreise, 2010). The depth to calcic horizon proxy was not applied to the PETM portion of the section because no calcic paleosols exist there. In general, the CIA-K and CALMAG precipitation proxies provide very similar results through the remainder of the study sections although the CALMAG values are approximately 100 mm greater than CIA-K (Fig. 11). The intercept of the linear fit is −42 but this is artificially low due to three data points with very low CALMAG values caused by high CaO contents. Several of our samples still contained appreciable CaO (5–14%) after acidification; we realize that the presence of this mineral phase impacts the CIA-K and CALMAG proxies for those samples, noting that the remainder of the sample set does not contain $CaCO_3$.

Below the PETM CIE, in the mid-Paleocene Mealla Fm, the CIA-K precipitation proxy shows that paleoprecipitation rates increased from ~600 ± 182 mm/yr at 30 m to ~1000 ± 182 mm/yr at 100 m in the section. The CALMAG values show a similar increasing trend, but with higher and slightly more variable calculated rates. CALMAG paleoprecipitation rates at the base of the section are ~600 ± 108 mm/yr increasing to ~1200 ± 108 mm/yr at the top of the 100 m of section. Depth-to-calcic-horizon paleoprecipitation estimates are highly variable. A slight increase is observed from 25 to 75 m; however, the average rate through the lowermost 100 m of section is ~300 ± 147 mm/yr. The depth-to-calcic horizon values are significantly lower than the other two proxies, likely due an underestimate of depth to the calcic horizon because the upper portion of the paleosol was removed by erosion associated with overlying channel sandstones.

Above the PETM CIE, variability in all the proxy estimates increases. The CIA-K proxy shows a slight increase from 240 to 390 m. The average paleoprecipitation rate for this portion of the section according to the CIA-K proxy is ~900 ± 182 mm/yr, though the CALMAG proxy levels out above the PETM. Some very low values due to low aluminum content and high calcium and magnesium content are present, samples in which diffuse carbonate still exists in the analyzed matrix. Overall, the average precipitation according to CALMAG is ~1050 ± 108 mm/yr through the same interval above the PETM CIE. Similarly to the Mealla Fm, the CALMAG proxy is most appropriate for the paleosols in the

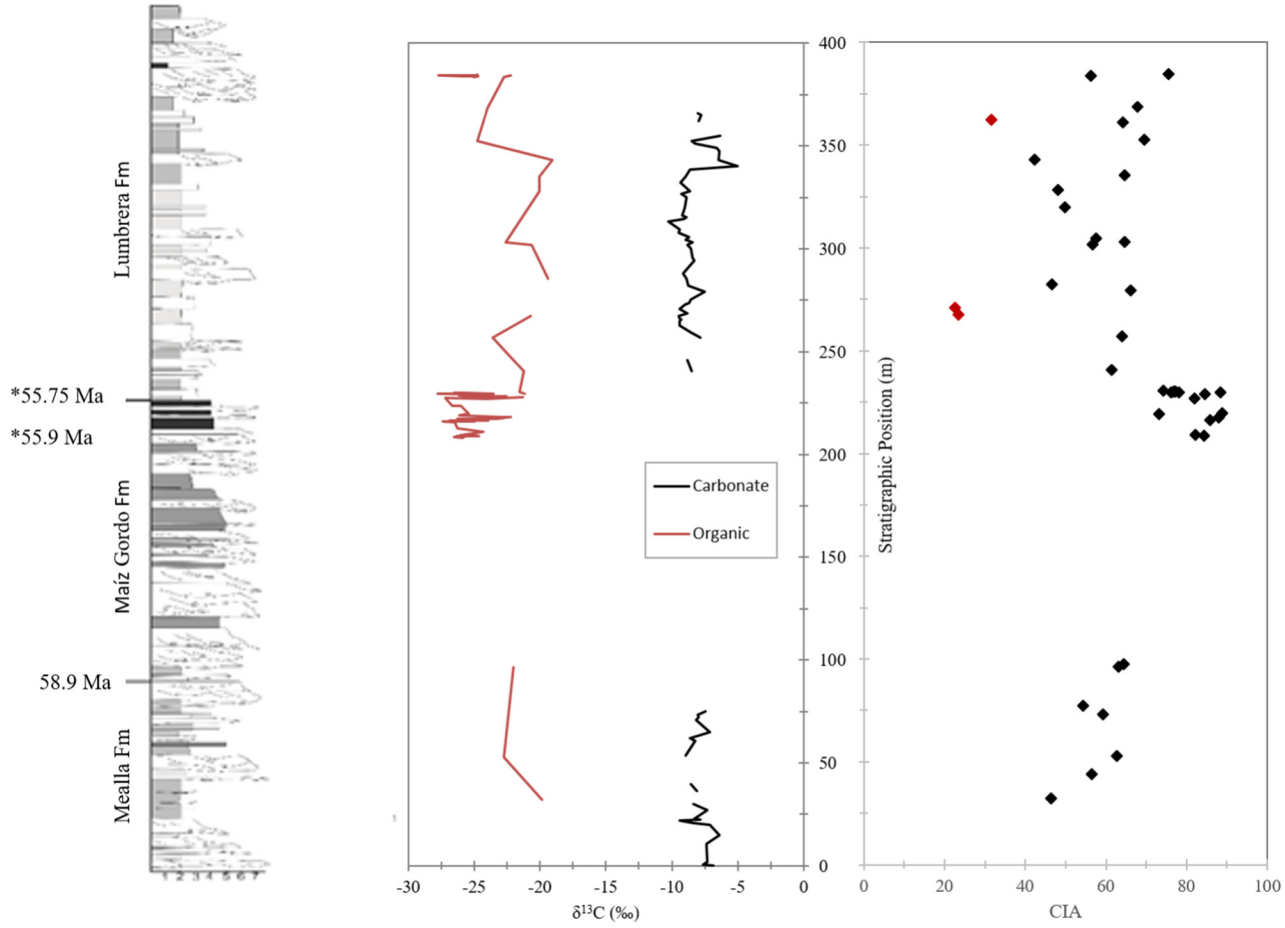

Fig. 9. Plot of carbon isotope data and CIA data with a stratigraphic column and the ages constrained by paleomagnetic studies of the Mealla Fm by Hyland et al. (2015) and analysis of the age of the onset and recovery of the CIE by Charles et al. (2011) denoted by an asterisk preceding the age. Note the peak in CIA data corresponding to the CIE in the Maiz Gordo Fm, supportive of other research (cited here) showing increased kaolinite content at the PETM. Red diamonds in the CIA plot indicate samples with significant CaO after acidification. (For interpretation of the references to color in this figure legend, the reader is referred to the web version of this article.)

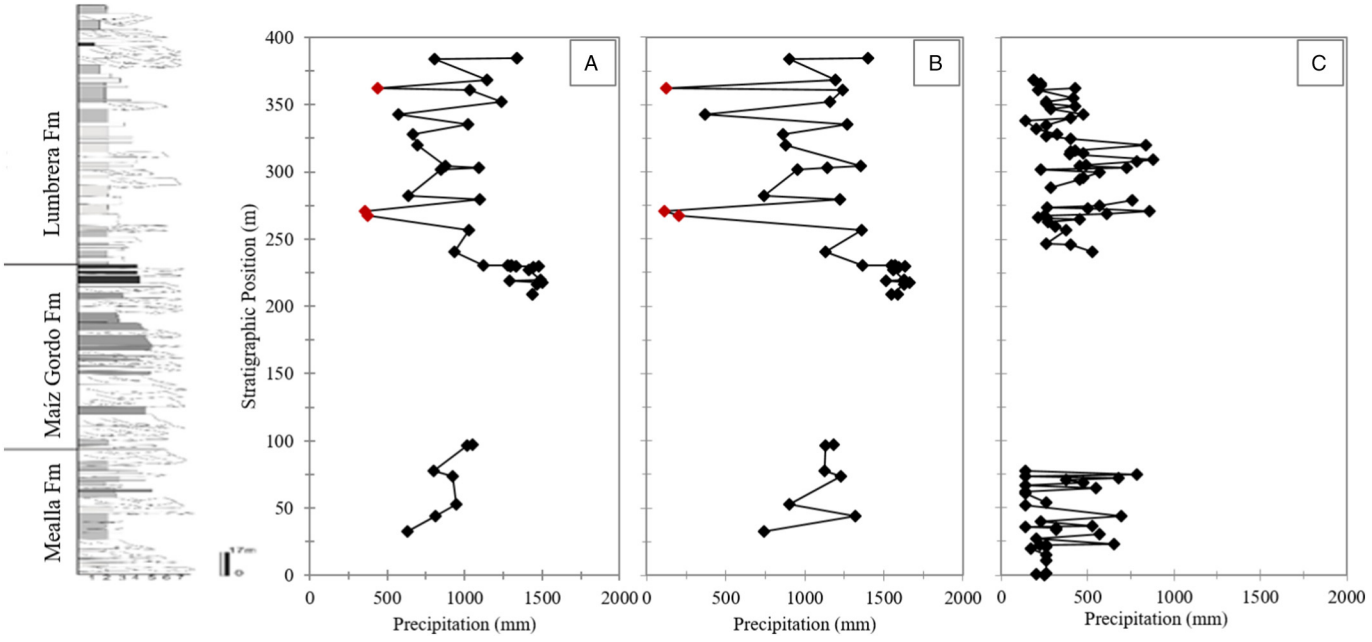

Fig. 10. Plot of stratigraphic column with paleoprecipitation rate calculated from A) CIA-K, B) CALMAG and C) depth-to-calcic horizon (CH) proxies. Red diamonds in A and B indicate samples that had high CaO values after acidification. (For interpretation of the references to color in this figure legend, the reader is referred to the web version of this article.)

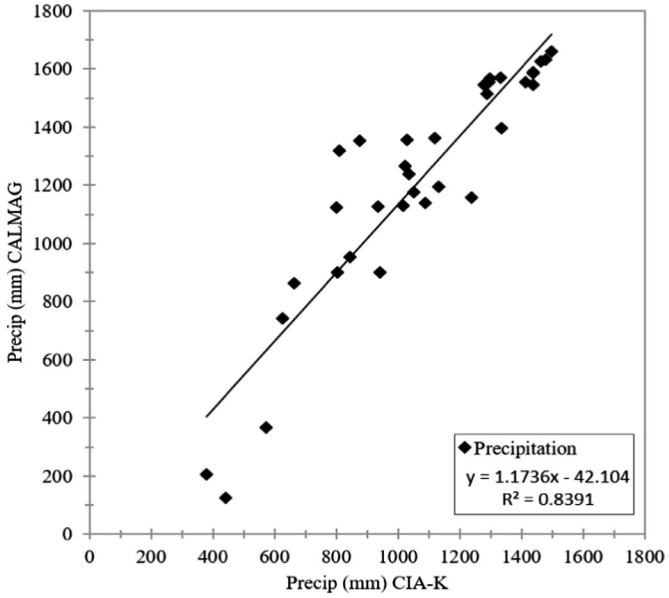

Fig. 11. Plot of calculated paleoprecipitation rate from the CALMAG proxy plotted against the calculated paleoprecipitation rate from the CIA-K proxy.

Lumbrera Fm. Paleoprecipitation rates predicted from the depth-to-calcic horizon method are much lower, averaging about 300 ± 147 mm/yr with peaks in paleoprecipitation rates of 900 ± 147 mm/yr at 260 and 310 m.

Both the CIA-K and CALMAG data show a clear increase in paleoprecipitation rate of ~500 mm/yr during the PETM. However, if the more appropriate CALMAG values for the Mealla and Lumbrera Fms paleosols are compared to the more appropriate CIA-K values for the PETM paleosols, then a precipitation rate increase of 400 mm/yr is determined. Similarly, Retallack (2005) reports a nearly 400 mm/yr increase in paleoprecipitation rate from a site in Utah using the depth to calcic horizon proxy. Retallack's increased paleoprecipitation rates differ from interpreted aridity leading up to the PETM in Bighorn Basin paleosols as reported by Kraus et al. (2013), and by Bowen and Beitler Bowen (2008) from their paleosol study site in central Utah. However the results from Kraus et al. (2013) and Bowen and Beitler Bowen (2008) do not contradict the trends seen in the Retallack (2005) study in which locally drier areas are suggested to have existed in the western U.S. from rain shadow effects of the Laramide Mountains.

Schmitz and Pujalte (2007) and Domingo et al. (2009) have hypothesized similar increases in precipitation rate during the PETM in Europe that resulted in the deposition of thick laterally extensive conglomerates dubbed "megafans", alluvial fan complexes that covered approximately 10^3–10^5 km^2. Similarly, in Colorado (western U.S.A), Foreman et al. (2012) reports a transition from paleosol-rich facies with thin laterally restricted sandstones to overlying thick laterally-extensive fluvial sandstones deposited during the PETM. Salta Group strata in Argentina probably display similar depositional processes induced by an enhanced hydrologic cycle during the PETM in that: 1) the Mealla and Maíz Gordo Fms display a transition to thick, quartz-rich coarse-grained sandstones and conglomerates, and 2) the strata are laterally extensive, correlatable across several hundred kilometers in the basin.

5.3. Paleotemperature

The paleothermometry ratio from Sheldon et al. (2002) and the PWI value from Gallagher and Sheldon (2013) are two additional weathering proxies: a low paleotemperature ratio or PWI value indicates that a soil has been extensively weathered from the initial parent material, whereas a high value indicates a soil in which weathering has not substantially altered the composition. Sheldon et al. (2002) and Gallagher and Sheldon (2013) related these proxies to mean annual temperature (MAT) based on correlations in modern soils, with the paleotemperature ratio and PWI values being inversely related to temperature. This inverse relationship exists because a more weathered soil can be the result of higher temperature; kinetics dictate that reactions occur faster at higher temperatures, thus weathering rate may be expected to increase.

Both the Sheldon et al. (2002) and Gallagher and Sheldon (2013) proxies were applied to interpreting Maíz Gordo Fm paleosols (see Fig. 12). The Sheldon et al. (2002) method predicts slightly higher paleotemperatures during the PETM, ~16 ± 4.4 °C, while the PWI method indicates PETM paleotemperatures of ~14–15 ± 2.1 °C. The Sheldon et al. (2002) proxy is a general paleotemperature proxy for all soil types whereas the Gallagher and Sheldon (2013) proxy focuses on three soil types: Ultisols, Alfisols and Inceptisols. Below and above the PETM section, the strata consists mostly of red calcic vertisols; thus the paleothermometry ratio was applied. The PETM section is marked by non-calcic paleosols that we tentatively consider to have been oxisols (and Ultisols and/or Inceptisols), so the PWI was used to reconstruct paleotemperature in the Maíz Gordo Fm.

In the Mealla Fm leading up to the PETM, paleotemperature estimates increase from ~6 ± 4.4 °C to ~10 ± 4.4 °C, with an average value of ~9 ± 4.4 °C. Above the PETM CIE in the Lumbrera Fm, from 240 m to the top of the section, paleotemperature displays an increase from ~8 ± 4.4 °C to ~11 ± 4.4 °C. The average temperature above the PETM is ~10 ± 4.4 °C, similar to the pre-PETM average paleotemperature estimate. The PWI paleotemperature calculation shows very similar results to the Sheldon et al. (2002) proxy for the section above and below the PETM. The two proxies have very similar results for the Mealla and Lumbrera Fms but in the Maíz Gordo Fm the difference in the proxy temperatures is a result of the different paleosol types described briefly above. These trends mimic the temperature curve presented in Zachos et al. (2001) in which temperature sharply increased at the PETM, and afterwards steadily increased towards the Early Eocene Climatic Optimum.

The PETM interval from the Salta Basin records a 5 ± 2.1 °C increase from paleotemperature estimates leading up to and after the PETM. This paleotemperature increase is of similar magnitude to the paleotemperature change reported by Wing et al. (2005) and others reporting change in sea surface paleotemperatures (Zachos et al., 2003). The maximum paleotemperature attained at the Argentina field site was ~15 °C whereas Wing et al. (2005) report a maximum temperature of 19.8 ± 3.1 °C during the PETM according to leaf margin analysis. These field sites were located at similar paleolatitudes: ~44°N for the Bighorn Basin (Wing et al., 2005) and ~40 ± 5°S for the Salta Basin in Argentina (Hyland et al., 2015).

6. Conclusions

Two stratigraphic sections were measured, described and sampled in the western part of the Salta Basin, northwestern Argentina. Strata in the basin span the PETM and include the Mealla, Maíz Gordo and Lumbrera Formations, characterized by a predominance of relatively coarse-grained fluvially deposited strata. Paleosols were described including measurements of depth to calcic horizon, thickness of calcic horizon, and the diameter and stage of development of calcareous nodules. Samples of paleosol matrix and nodules were collected for geochemical and isotopic analyses. Analyses included organic matter and carbonate carbon isotopes, major oxides and trace elements. The data was used to generate carbon isotopic profiles of the composite sections along with plots of Chemical Index of Alteration (CIA), CIA-K, CALMAG, paleosol weathering index, and paleothermometry ratio.

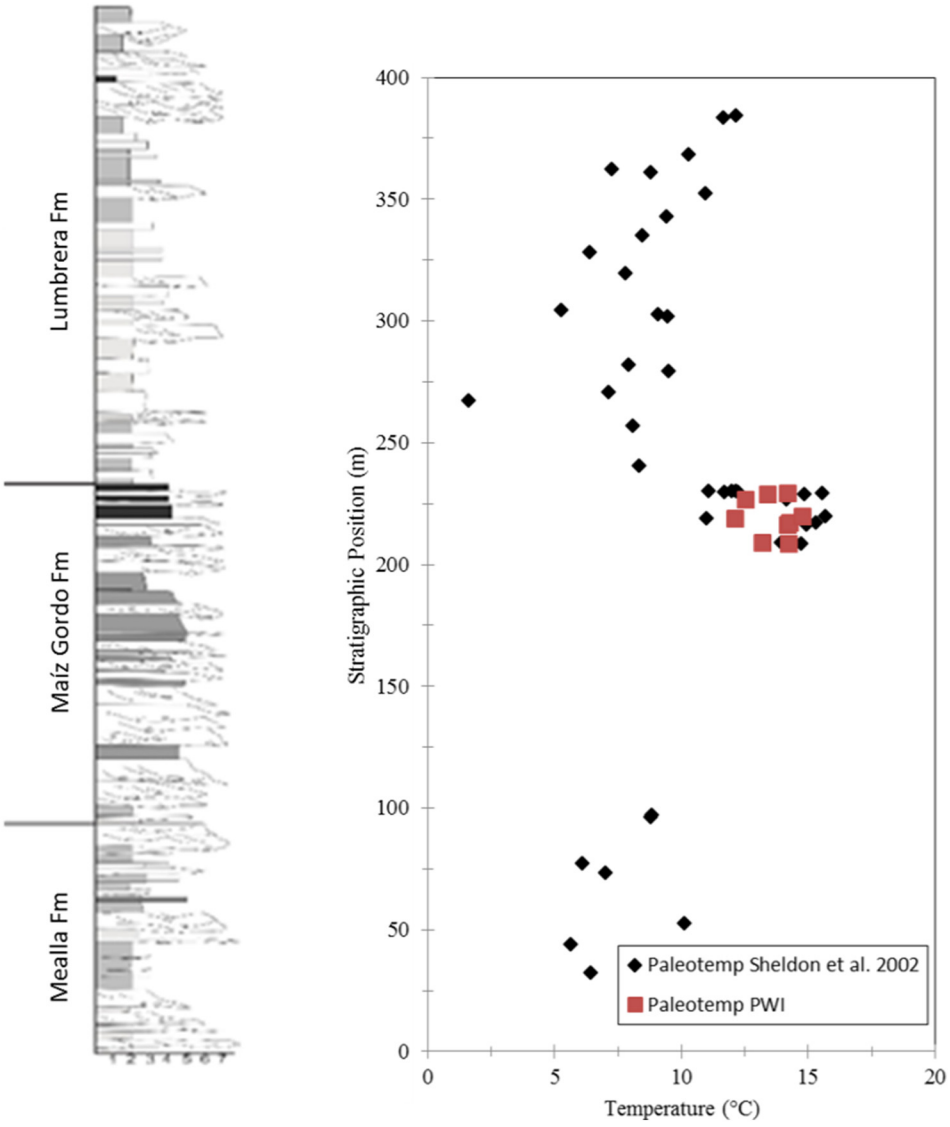

Fig. 12. Plot of paleotemperature calculated using equations from Sheldon et al. (2002) in black and from Gallagher and Sheldon (2013) in red. (For interpretation of the references to color in this figure legend, the reader is referred to the web version of this article.)

An ~−6‰ organic matter CIE at the top of the Maíz Gordo Fm is interpreted to record the PETM in the formation. This CIE contains three shifts, the oldest of which is a −3‰ shift, while the overlying second and third shifts are each about −5–6‰. Our preferred interpretation is that the initial −3‰ shift in the Maíz Gordo Fm correlates to the −3‰ POE shift identified by Bowen et al. (2015) from coeval sections in Wyoming, while the overlying −6‰ excursion in the Maíz Gordo Fm matches the primary −6‰ CIE observed by Bowen et al. (2015). Notably different from the Bowen et al. (2015) carbon isotope data is the presence of a third excursion in the Salta Basin record, of equal magnitude to the second excursion. Additional notable CIEs observed in the underlying Mealla and overlying Lumbrera Fms likely mark mid-Paleocene and early Eocene hyperthermal events, respectively. The match in total number of CIEs in the Lumbrera Fm and early Eocene marine strata is notable.

Average calculated paleoprecipitation rates are ~1100 ± 108 mm/yr leading up to the PETM. During the PETM the calculated precipitation rate increases to ~1500 ± 182 mm/yr. Paleoprecipitation rates begin to decrease after the PETM and average ~ 1050 ± 108 mm/yr. Paleotemperature calculations show a similar trend of increasing temperature up to the PETM, from ~6 ± 4.4 °C to ~10 ± 4.4 °C, with an average value of ~9 ± 4.4 °C, followed by a spike in paleotemperature during the PETM to an average value of ~14–15 ± 2.1 °C. Above the PETM CIE in the Lumbrera Fm, paleotemperature displays an increase from ~8 ± 4.4 °C to ~11 ± 4.4 °C, averaging ~10 ± 4.4 °C, similar to the pre-PETM average paleotemperature estimate. The section presented here mimics the temperature curve presented in Zachos et al. (2001) in which temperature sharply increased at the PETM, dropped and then subsequently steadily increased towards the Early Eocene Climatic Optimum.

Acknowledgements

The authors thank the Ministerio de Ambiente y Desarrollo Sustentable, Salta Province, the Programa Areas Protegidas, Secretaria de Ambiente, Salta Government and the guards of the Reserva Manejada Quebrada de las Conchas for permission to work in the Quebrada de las Conchas Park. Funding for this project was provided by the Penn State Department of Geosciences for senior thesis research.

Appendix A

Table 1A
Major oxide data presented in molar %.

TSW 09	Depth (m)	Al_2O_3	CaO	Fe_2O_3T	K_2O	MgO	MnO	Na_2O	P_2O_5	SiO_2	TiO_2	Total
143	32.2	11.12	6.370	2.218	2.706	3.886	0.0887	3.8291	0.0782	69.71	0.6035	100.6
146	44.15	8.587	1.192	0.858	1.945	1.307	0.0260	3.4588	0.1120	82.51	0.2840	100.3
148	52.8	12.64	2.602	2.213	2.727	6.186	0.0675	2.1881	0.0945	71.28	0.6198	100.6
155	73.25	7.820	1.008	1.040	2.224	1.846	0.0261	2.1226	0.0769	83.84	0.3013	100.3
157	77.35	7.916	1.883	1.131	2.294	1.705	0.0368	2.5030	0.2347	82.30	0.3168	100.3
158	96.35	10.17	1.268	1.956	2.775	3.293	0.0583	1.8947	0.1561	78.43	0.5154	100.5
159	97.35	9.551	0.908	1.634	2.582	2.958	0.0558	1.7924	0.0904	80.43	0.4724	100.5
16	208.5	10.39	0.473	1.324	1.210	0.786	0.0112	0.2331	0.0321	85.54	0.6548	100.7
19	209.1	11.88	0.408	1.911	1.759	1.312	0.0262	0.4057	0.0391	82.26	0.7951	100.8
26	216.3	11.95	0.449	4.506	1.294	0.733	0.0258	0.2440	0.0522	80.74	0.5928	100.6
31	217.3	13.98	0.411	1.767	1.276	0.728	0.0090	0.2188	0.0356	81.57	0.8905	100.9
37	219.1	10.79	0.303	1.809	2.522	1.450	0.0189	1.1479	0.0381	81.92	0.5219	100.5
38A	219.7	12.30	0.458	1.290	0.955	0.758	0.0087	0.1325	0.0244	84.07	0.7593	100.8
43	226.8	16.09	0.792	3.161	2.300	1.427	0.0161	0.4624	0.0599	75.69	0.9636	101.0
48	228.8	14.74	0.723	2.904	1.677	1.035	0.0147	0.2782	0.0372	78.59	0.9025	100.9
52	229.6	14.48	0.495	1.929	1.121	0.903	0.0091	0.2636	0.0282	80.77	0.9390	100.9
160	229.65	12.10	0.090	1.579	2.022	1.484	0.0082	1.2881	0.0129	81.42	0.7134	100.7
161	229.85	12.20	0.125	3.701	2.211	1.576	0.0162	1.4890	0.0612	78.62	0.7116	100.7
162	230.05	12.52	0.204	2.048	2.060	1.451	0.0108	1.4189	0.0571	80.23	0.7246	100.7
163	230.25	12.14	0.175	3.597	1.966	1.573	0.0135	1.5247	0.0521	78.96	0.7025	100.7
165	230.4	13.01	0.138	2.487	1.482	3.238	0.0109	2.8891	0.0324	76.71	0.7932	100.8
70	240.6	10.67	1.550	2.281	2.608	3.256	0.0856	2.5730	0.0591	76.92	0.7099	100.7
73	256.85	10.37	0.657	1.896	2.715	2.092	0.0484	2.4549	0.0548	79.71	0.5750	100.6
79	267.25	5.920	14.17	0.301	3.105	0.799	0.0539	1.9139	0.0711	73.67	0.0655	100.1
81	270.65	5.199	14.79	0.666	1.532	1.512	0.0736	1.3225	0.1011	74.81	0.2200	100.2
85	279.3	10.72	0.989	2.235	2.841	2.949	0.0790	1.6688	0.0870	78.43	0.6459	100.6
85A	282.3	10.65	6.837	2.208	2.679	3.033	0.1169	2.7274	0.0525	71.70	0.6400	100.6
90	301.85	8.732	2.940	1.791	2.364	2.581	0.1484	1.3421	0.0390	80.06	0.5494	100.5
91	303	11.55	1.217	2.528	3.400	3.860	0.2049	1.7229	0.1560	75.36	0.6435	100.6
92	304.55	7.608	0.671	1.055	2.167	1.356	0.0242	2.7875	0.1078	84.22	0.3357	100.3
100	319.85	8.568	4.215	1.307	2.237	2.027	0.1229	2.1587	0.0791	79.28	0.4851	100.5
103	328.15	9.606	4.717	1.934	2.522	2.447	0.2160	3.1392	0.0737	75.34	0.5902	100.6
105	335.15	11.09	0.770	2.124	2.697	2.909	0.0649	2.6115	0.0659	77.67	0.6358	100.6
106	342.95	7.419	6.940	1.300	1.918	6.539	0.2015	1.2519	0.0760	74.36	0.4158	100.4
110	352.45	12.63	1.196	3.009	3.490	4.149	0.1302	0.8457	0.0842	74.47	0.8274	100.8
112	361.05	10.22	1.007	1.847	2.678	2.595	0.0392	2.0208	0.1336	79.46	0.5833	100.6
113	362.25	8.399	13.48	1.840	2.074	12.069	0.3737	2.4808	0.0781	59.21	0.5604	100.6
116	368.5	11.27	1.075	2.660	2.902	3.327	0.0854	1.3767	0.1450	77.15	0.7225	100.7
117	383.7	10.04	4.722	1.793	2.263	2.270	0.0640	0.8050	0.0445	78.00	0.5758	100.6
121	384.5	10.31	0.490	1.917	2.192	1.944	0.0442	0.6682	0.0478	82.39	0.6114	100.6

Table 1B
Carbon isotope data with depth.

Depth (m)	$CaCO_3$ $\delta^{13}C$	Corg $\delta^{13}C$	Depth (m)	$CaCO_3$ $\delta^{13}C$	Corg $\delta^{13}C$	Depth (m)	CaCO3 $\delta^{13}C$	Corg $\delta^{13}C$
0	−6.86		216.9		−25.3331	273.7	−8.72	
0.7	−7.635		217.1		−25.6267	275.25	−8.59	
1.7	−7.31		217.3		−26.3063	279.3	−7.525	
10.8	−7.41		217.5		−23.3225	282.3	−8.74	
15	−6.38		217.7		−22.7228	285.3	−8.87	−19.4
19.7	−7.12		217.9		−23.2257	288.1	−9.14	
20.9	−8.34		218.1		−22.1983	294.35	−8.3	
22.2	−9.42		218.3		−22.915	295.65	−8.445	
22.55	−7.87		219.1		−25.2919	300.05	−8.55	
22.9	−8.33		219.7		−25.3992	301.85	−8.82	
27.1	−7.33		223.6		−25.9879	303	−8.42	−20.6
30.1	−8.35		223.8		−26.6982	304.55	−8.97	−22.6
32.2			227.4		−27.2053	305.55	−8.69	
36.35	−8.1		227.6		−26.8508	307.75	−9.48	
39.75	−8.54		226.8		−22.2661	309.55	−9.4	
44.15			228		−21.2828	313.35	−10.25	
52.15	−8.31		228.2		−22.5213	314.35	−9.07	
52.8			228.4		−25.3006	315.35	−8.91	
53.65	−8.95		228.6		−26.1184	316.35	−9.2	
60.65	−8.23		228.8		−26.6617	319.85	−9.01	
62.05	−8.62		229		−25.2814	325.15	−8.86	
64.95	−7.135		229.2		−24.5053	326.65	−9.25	
70.75	−8.16		229.4		−27.7838	328.15	−8.64	−20
72.25	−8		229.6		−24.1845	332.1	−9.37	
73.25	−8.01	−19.9	229.65		−21.2	335.15	−8.95	−20.1

(continued on next page)

Table 1B (*continued*)

Depth (m)	$CaCO_3$ $\delta^{13}C$	Corg $\delta^{13}C$	Depth (m)	$CaCO_3$ $\delta^{13}C$	Corg $\delta^{13}C$	Depth (m)	CaCO3 $\delta^{13}C$	Corg $\delta^{13}C$
74.95	−7.47		229.8		−25.7149	338.55	−8.64	
77.35			229.85			340.05	−4.995	
96.35		−22	230		−26.5326	342.95	−6.435	−19.1
97.35			230.05			347.35	−6.39	
208		−25.9167	230.25			348.85	−6.585	
208.3		−26.5168	230.4		−21.6	350.95	−8.245	
208.5		−25.6893	240.6	−8.48	−21.3	352.45	−8.505	−24.8
208.7		−26.3418	246	−8.81		355.05	−6.36	
208.9		−24.6267	246.7			361.05		
209.1		−23.9145	256.85	−7.865	−23.6	362.25	−7.96	
209.3		−26.1132	259.35	−8.56		364.85	−7.8	
211.1		−24.3002	262.6	−9.39		366	−8.06	
212.6		−26.2869	264.78	−9.43		368.5		−24
215.7		−26.4514	265.53	−9.27		383.7		−25.0338
215.9		−27.4054	265.93	−9.42		383.9		−24.7046
216.1		−24.9681	267.25	−9.49	−20.7	384.1		−25.8572
216.3		−26.588	268.85	−8.83		384.3		−27.7001
216.5		−23.9027	270.65	−9.43		384.5		−24.797
216.7		−24.8409	272.75	−9.05		384.7		−24.7539

References

Adams, J.S., Kraus, M.J., Wing, S.L., 2011. Evaluating the use of weathering indices for determining mean annual precipitation in the ancient stratigraphic record. Palaeogeogr. Palaeoclimatol. Palaeoecol. 309 (3–4), 358–366.

Aitchison, J.C., Ali, J.R., Davis, A.M., 2007. When and where did India and Asia collide? J. Geophys. Res. 112, B05423.

Blakey, R., 2014. Global Paleogeography (Colorado Plateau Geosystems).

Bowen, G.J., Beitler Bowen, B., 2008. Mechanisms of PETM global change constrained by a new record from Central Utah. Geology 36 (5), 379–382.

Bowen, G.J., Beerling, D.J., Koch, P.L., Zachos, J.C., Quattlebaum, T., 2004. A humid climate state during the Palaeocene/Eocene Thermal Maximum. Nature 432 (7016), 495–499.

Bowen, G.J., Maibauer, B.J., Kraus, M.J., Röhl, U., Westerhold, T., Steimke, A., Gingerich, P.D., Wing, S.L., Clyde, W.C., 2015. Two massive, rapid releases of carbon during the onset of the Palaeocene-Eocene Thermal Maximum. Nat. Geosci. 8 (1), 44–47.

Bralower, T.J., Thomas, D.J., Zachos, J.C., Hirschmann, M.M., Röhl, U., Sigurdsson, H., Thomas, E., Whitney, D.L., 1997. High resolution record of the late Paleocene Thermal Maximum and circum-Caribbean volcanism: is there a causal link? Geology 25, 963–966.

Charles, A.J., Condon, D.J., Harding, I.C., Pälike, H., Marshall, J.E.A., Cui, Y., Kump, L., Croudace, I.W., 2011. Constraints on the numerical age of the Paleocene Eocene boundary. Geochem. Geophys. Geosyst. 12 (6), Q0AA17.

Clechenko, E., Kelly, D., Harrington, G., Stiles, C., 2007. Terrestrial records of a regional weathering profile at the Paleocene-Eocene boundary in the Williston Basin of North Dakota. GSA Bulletin 119 (3–4), 428–442.

Cramer, B.S., Wright, J.D., Kent, D.V., Aubry, M.P., 2003. Orbital climate forcing of $\delta^{13}C$ excursions in the late Paleocene-early Eocene (chrons C24n–C25n). Paleoceanography 18 (4).

Cui, Y., Kump, L.R., Ridgwell, A.J., Junium, C.K., Diefendorf, A.F., Freeman, K.H., Urban, N.M., Harding, I.C., 2011. Slow release of fossil carbon during the Paleocene Eocene Thermal Maximum. Nat. Geosci. 4 (7), 481–485.

del Papa, C.E., 1999. Sedimentation on a ramp type lake margin: Paleocene-Eocene Maíz Gordo Formation, northwestern Argentina. J. S. Am. Earth Sci. 12 (4), 389–400.

del Papa, C., Kirschbaum, A., Powell, J., Brod, A., Hongn, F., Pimentel, M., 2010. Sedimentological, geochemical and paleontological insights applied to continental omission surfaces: a new approach for reconstructing an Eocene foreland basin in NW Argentina. J. S. Am. Earth Sci. 29 (2), 327–345.

Dickens, G.R., O'Neil, J.R., Rea, D.K., Owen, R.M., 1995. Dissociation of oceanic methane hydrate as a cause of the carbon isotope excursion at the end of the Paleocene. Paleoceanography 10 (6), 965–971.

Domingo, L., López Martinez, N., Leng, M.J., Grimes, S.T., 2009. The Paleocene Eocene Thermal Maximum record in the organic matter of the Claret and Tendruy continental sections (South central Pyrenees, Lleida, Spain). Earth Planet. Sci. Lett. 281 (3), 226–237.

Fedo, C., Nesbitt, H., Young, G., 1995. Unraveling the effects of potassium metasomatism in sedimentary rocks and paleosols, with implications for paleoweathering conditions and provenance. Geology 23, 921–924.

Foreman, B.Z., Heller, P.L., Clementz, M.T., 2012. Fluvial response to abrupt global warming at the Palaeocene/Eocene boundary. Nature 490 (7422), 92–95.

Gallagher, T.M., Sheldon, N.D., 2013. A new paleothermometer for the forest paleosols and its implications for Cenozoic climate. Geology 41 (6), 647–650.

Garel, S., Schnyder, J., Jacob, J., Dupuis, C., Boussafir, M., Le Milbeau, C., Storme, J.Y., Iakovleva, A.I., Yans, J., Baudin, F., Fléhoc, C., Quesnel, F., 2013. Paleohydrological and paleoenvironmental changes recorded in terrestrial sediments of the Paleocene Eocene boundary (Normandy, France). Palaeogeogr. Palaeoclimatol. Palaeoecol. 376, 184–199.

Gregory-Wodzicki, K.M., 2000. Uplift history of the central and northern Andes: a review. Geol. Soc. Am. Bull. 112 (7), 1091–1105.

Hyland, E.G., Sheldon, N.D., Cotton, J.M., 2015. Terrestrial evidence for a two stage mid Paleocene biotic event. Palaeogeogr. Palaeoclimatol. Palaeoecol. 417, 371–378.

Kennett, J.P., Stott, L.D., 1991. Abrupt deep sea warming, palaeoceanographic changes and benthic extinctions at the end of the Palaeocene. Nature 252 (6341), 225–229.

Kent, D.V., Cramer, B.S., Lanci, L., Wang, D., Wright, J.D., Van der Voo, R., 2003. A case for a comet impact trigger for the Paleocene/Eocene Thermal Maximum and carbon isotope excursion. Earth Planet. Sci. Lett. 211 (1–2), 13–26.

Koch, P.L., Zachos, J.C., Dettman, D.L., 1995. Stable isotope stratigraphy and paleoclimatology of the Paleogene Bighorn Basin (Wyoming, USA). Palaeogeogr. Palaeoclimatol. Palaeoecol. 115 (1), 61–89.

Koch, P., Clyde, W., Hepple, R., Fogel, M., Wing, S., Zachos, J., 2003. Carbon and Oxygen Isotope Records from Paleosols Spanning the Paleocene-Eocene Boundary, Bighorn Basin, Wyoming. In: Wing, S., Gingerich, P., Schmitz, B., Thomas, E. (Eds.), Causes and Consequences of Globally Warm Climates in the Earl Paleogene. GSA Spec. Pap Vol. 369, pp. 49–64.

Kraus, M.J., Riggins, S., 2007. Transient drying during the Paleocene-Eocene Thermal Maximum (PETM): analysis of paleosols in the Bighorn Basin, Wyoming. Palaeogeogr. Palaeoclimatol. Palaeoecol. 245 (3–4), 444–461.

Kraus, M.J., McInerney, F.A., Wing, S.L., Secord, R., Baczynski, A.A., Block, J.I., 2013. Paleohydrologic response to continental warming during the Paleocene Eocene Thermal Maximum, Bighorn Basin, Wyoming. Palaeogeogr. Palaeoclimatol. Palaeoecol. 370, 196–208.

Mack, Greg H., James, W. Calvin, 1992. Paleosols for Sedimentologists, Geological Society of America Short Course Notes, Presented on the Occasion of the Annual Meeting of the Geological Society of America, October 26–29, 1992, Cincinnati, Ohio (127 pp).

Mack, Greg H., James, W. Calvin, Monger, H. Curtis, 1993. Classification of paleosols. Geol. Soc. Am. Bull. 105, 129–136.

Marquillas, R., del Papa, C., Sabino, I., 2005. Sedimentary aspects and paleoenvironmental evolution of a rift basin: Salta group (cretaceous-Paleogene), northwestern Argentina. Int. J. Earth Sci. 94 (1), 94–113.

Maynard, J.B., 1992. Chemistry of modern soils as a guide to interpreting Precambrian paleosols. The Journal of Geology 100 (3), 279–289.

Miller, K.G., Fairbanks, R.G., Mountain, G.S., 1987. Tertiary oxygen isotope synthesis, sea level history and continental margin erosion. Paleoceanography 2 (1), 1–19.

Moore, E.A., Kurtz, A.C., 2008. Black carbon in Paleocene-Eocene boundary sediments: a test of biomass combustion as the PETM trigger. Palaeogeogr. Palaeoclimatol. Palaeoecol. 267 (1–2), 147–152.

Nesbitt, H., Young, G., 1982. Early Proterozoic climates and plate motions inferred from major element chemistry of lutites. Nature 199, 715–717.

Nicolo, M.J., Dickens, G.R., Hollis, C.J., Zachos, J.C., 2007. Multiple early Eocene hyperthermals: their sedimentary expression on the new Zealand continental margin and in the deep sea. Geology 35 (8), 699–702.

Nordt, L.C., Dreise, S.D., 2010. New weathering index improves paleorainfall estimates from vertisols. Geology 38 (5), 407–410.

Quattrochio, M.E., Volkheimer, W., Marquillas, R.A., Salfity, J.A., 2005. Palynostratigraphy, palaeobiogeography and evolutionary significance of the late Senonian and early Paleogene palynofloras of the Salta group, northern Argentina. Rev. Esp. Micropaleontol. 37 (2), 259–272.

Retallack, G.J., 2005. Pedogenic carbonate proxies for amount and seasonality of precipitation in paleosols. Geology 22 (4), 333–336.

Robert, C., Kennett, J., 1994. Antarctic subtropical humid episode at the Paleocene-Eocene boundary: clay mineral evidence. Geology 22, 211–214.

Röhl, U., Westerhold, T., Bralower, T.J., Zachos, J.C., 2007. On the duration of the Paleocene Eocene Thermal Maximum (PETM). Geochem. Geophys. Geosyst. 8 (12), Q12002.

Schmitz, B., Pujalte, V., 2007. Abrupt increase in seasonal extreme precipitation at the Paleocene Eocene boundary. Geology 35 (3), 215–218.

Sempere, T., Butler, R.F., Richards, D.R., Marshall, L.G., Sharp, W., Swisher, C.C., 1997. Stratigraphy and chronology of Upper Cretaceous-lower Paleogene strata in Bolivia and northwest Argentina. Geol. Soc. Am. Bull. 109 (6), 709–727.

Sheldon, N.D., Retallack, G.J., Tanaka, S., 2002. Geochemical climofunctions from north American soils and application to paleosols across the Eocene Oligocene boundary in Oregon. J. Geol. 110, 687–696.
Smith, F.A., Wing, S.L., Freeman, K.H., 2007. Magnitude of the carbon isotope excursion at the Paleocene-Eocene Thermal Maximum: the role of plant community change. Earth Planet. Sci. Lett. 262 (1–2), 50–65.
White, P.D., Schiebout, J., 2008. Paleogene paleosols and changes in pedogenesis during the initial Eocene Thermal Maximum: Big Bend National Park, Texas, USA. Geol. Soc. Am. Bull. 12 (11–12), 1347–1361.
Wing, S.L., Harrington, G.J., Smith, F.A., Bloch, J.L., Boyer, D.M., Freeman, K.H., 2005. Transient floral change and rapid global warming at the Paleocene Eocene boundary. Science 310 (5750), 993–996.
Woodburne, M.O., Gunnell, G.F., Stucky, R.K., Berggren, W.A., 2009. Climate directly influences Eocene mammal faunal dynamics in North America. Proc. Natl. Acad. Sci. U. S. A. 106 (32), 13399–13403.
Wooldridge, C.L., Hickin, E.J., 2005. Radar architecture and evolution of channel bars in wandering gravel-bed rivers: Fraser and Squamish rivers, British Columbia, Canada. J. Sediment. Res. 75, 844–860.
Zachos, J., Pagani, M., Sloam, L., Thomas, E., Billups, K., 2001. Trends, rhythms, aberrations in global climate 65 Ma to present. Science 292 (5517), 686–693.
Zachos, J.C., Wara, M.W., Bohaty, S., Delaney, M.L., Petrizzo, M.R., Brill, A., Bralower, T.J., Premoli, Silva I., 2003. A transient rise in tropical sea surface temperature during the Paleocene Eocene Thermal Maximum. Science 302 (5650), 1551–1554.
Zachos, J.C., Röhl, U., Schellenberg, S.A., Sluijs, A., Hodell, D.A., Kelly, D.C., Thomas, E., Nicolo, M., Raffi, I., Lourens, L.J., McCarren, H.M., Kroon, D., 2005. Rapid acidification of the ocean during the Paleocene Eocene Thermal Maximum. Science 308 (5728), 1611–1615.
Zachos, J.C., McCarren, H., Murphy, B., Röhl, U., Westerhold, T., 2010. Tempo and scale of late Paleocene and early Eocene carbon isotope cycles: implications for the origin of hyperthermals. Earth Planet. Sci. Lett. 299 (1–2), 242–249.
Zeebe, R., Ridgwell, A., Zachos, J., 2016. Anthropogenic carbon release rate unprecedented during the past 66 million years. Nat. Geosci. 9, 325–329.